Novel continuous limit analysis modeling with deformable polygon discretization

Yiwei Hua[1*] and Gabriele Milani[2]

[1] Department of Architecture, Built Environment and Construction Engineering, Politecnico di Milano, Piazza Leonardo da Vinci 32, 20133 Milan, Italy
*yiwei.hua@polimi.it

Abstract. Continuous-modeling limit analysis is one of the promising tools for analyzing the failure of soil-like material. Standard formulation comes up from the idea of finite element analysis. Usually, in this approach, the freedom of the degrees is assigned at the nodes. However, such a theory will limit the shape of the elements, which is only applicable to solving triangular mesh. In this paper, we propose a novel approach based on the idea of continuous modeling limit analysis. Here, all the variables are assigned at the centroid of the element, through which the approach can be easily extended to consider arbitrary polygon discretization. Assuming constant strain distribution, we first derive the geometric compatibility for arbitrary polygon deformable elements. Then, the flow rule for the plasticity in the elements is investigated. Implementing the proposed theory, the classical strip footing problem is solved as a benchmark study, with consideration of one triangular mesh and two polygon mesh. The results show that the load predicted by polygon mesh is overestimated, indicating the occurrence of the locking in the elements. However, the strain rate distribution predicted by the polygon mesh is more uniform.

Keywords: Limit analysis, Soil-like material, Polygon mesh, Voronoi, Continuous modelling.

1 Introduction

Limit analysis is one of the important approaches to analyzing the failure of the soil-like material, through which the collapse mechanism and the ultimate load of the continuum can be quickly predicted in a single step. Utilizing this approach, many geomechanics problems [1–4] as well as soil-structure interactions [5–9] can be investigated. In these contributions, the soil was commonly regarded as a deformable continuum discretized by small elements. The governing formulations for these elements were developed based on the idea of Finite Element Method (FEM). Usually, linear distribution for the displacement (velocity) within the elements was assumed, and as we know in finite element theory, such shape function can be easily incorporated with triangular elements. Nevertheless, the triangular mesh can only produce straight cracking, which should deviate from reality. Polygon elements should be more suitable to obtain a more realistic zig-zag crack propagation. However, proposing a de-

formable polygon element is a quite complex problem because it requires a cautious design of the shape function. In this paper, we develop a novel deformable polygon element with constant-strain distribution, which could become an alternative when implementing the limit analysis.

The formulation is established based on the Upper Bound theory. We first propose the geometric compatibility condition for arbitrary polygon elements with constant strain. Then, the flow rule condition describing the plastic behavior in the elements is investigated. Here, we use the associated Mohr-Coulomb model for both the sliding behavior at interfaces and the plastic behavior in elements. In this paper, we present the collapse analysis of the classical strip footing problem as an implementation of the proposed theory. First, the collapse of the strip footing with a mesh of triangular elements is analyzed as a benchmark to verify the precision of the proposed theory. Then, the performance of polygon elements is investigated, with consideration of two different types of discretization. We finally conclude the paper with some discussions of these results.

2 Methodology

In this section, we propose a deformable element with arbitrary polygon shape for limit analysis. A constant strain field is assumed. The formulation is established based on Upper Bound (UB) theorem. Now let us first investigate the geometric compatibility condition.

$$\begin{cases} \dot{\varepsilon}_x(x,y) = \dfrac{\partial \dot{u}_x(x,y)}{\partial x},\ \dot{\varepsilon}_y(x,y) = \dfrac{\partial \dot{u}_y(x,y)}{\partial y} \\ \dot{\varepsilon}_{xy}(x,y) = \dfrac{1}{2}\left(\dfrac{\partial \dot{u}_y(x,y)}{\partial x} + \dfrac{\partial \dot{u}_x(x,y)}{\partial y} \right) \\ \omega(x,y) = \dfrac{1}{2}\left(\dfrac{\partial \dot{u}_y(x,y)}{\partial x} - \dfrac{\partial \dot{u}_x(x,y)}{\partial y} \right) \end{cases} \tag{1}$$

$$\begin{cases} \dot{\varepsilon}_x(x,y) \equiv \dot{\varepsilon}_x^i,\ \dot{\varepsilon}_y(x,y) \equiv \dot{\varepsilon}_y^i,\ \dot{\varepsilon}_{xy}(x,y) \equiv \dot{\varepsilon}_{xy}^i,\ \omega(x,y) \equiv \omega^i \\ \dot{u}_x(0,0) = \dot{u}_x^i,\ \dot{u}_y(0,0) = \dot{u}_y^i \end{cases} \tag{2}$$

According to the elastic theory, the strain rate field can be derived from the deviation of the velocity field (Eq. (1)). The known stain rates and velocities at the centroid of the element act as a boundary condition of partial differential equations (2), taking the centroid as the original.

As a result, the velocity field in a specific polygon element *i* can be explicitly given as follows (Eq. (3)).

$$\mathbf{u}^i\left(x,y\right)=\begin{bmatrix}\dot{u}_x\left(x,y\right)\\ \dot{u}_y\left(x,y\right)\end{bmatrix}=\begin{bmatrix}\dot{\varepsilon}_x^i x+\left(\dot{\varepsilon}_{xy}^i-\omega^i\right)y+\dot{u}_x^i\\ \dot{\varepsilon}_y^i y+\left(\dot{\varepsilon}_{xy}^i+\omega^i\right)x+\dot{u}_y^i\end{bmatrix} \tag{3}$$

We now proceed to consider two adjacent blocks a and b, with a shared joint j (**Fig. 1**) and investigate how to calculate the velocity discontinuities $\mathbf{q}_j$ at this joint based on centroid variables ($\mathbf{u}^i$ and $\boldsymbol{\varepsilon}^i$, $i = a, b$).

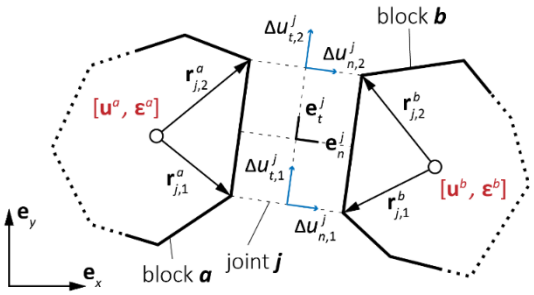

Fig. 1. Joint j with two adjacent polygon blocks a and b: calculation of velocity discontinuities.

Based on the known velocity field, for block i, the velocities at vertices 1 and 2 associated with joint j under the global frame can be calculated (Eq. (4), written as a matrix form).

$$\begin{aligned}\mathbf{u}_j^i&=\begin{bmatrix}\dot{u}_{x,1}^i & \dot{u}_{y,1}^i & \dot{u}_{x,2}^i & \dot{u}_{y,2}^i\end{bmatrix}^T=\left(\mathbf{B}_{j,u}^i\right)^T\mathbf{u}^i+\left(\mathbf{B}_{j,\varepsilon}^i\right)^T\boldsymbol{\varepsilon}^i\\&=\begin{bmatrix}1&0&-y_1^i\\0&1&x_1^i\\1&0&-y_2^i\\0&1&x_2^i\end{bmatrix}\begin{bmatrix}\dot{u}_x^i\\\dot{u}_y^i\\\omega_c^i\end{bmatrix}+\begin{bmatrix}x_1^i&0&y_1^i\\0&y_1^i&x_1^i\\x_2^i&0&y_2^i\\0&y_2^i&x_2^i\end{bmatrix}\begin{bmatrix}\dot{\varepsilon}_x^i\\\dot{\varepsilon}_y^i\\\dot{\varepsilon}_{xy}^i\end{bmatrix}\end{aligned} \tag{4}$$

$$\begin{aligned}\mathbf{q}_j&=\begin{bmatrix}\Delta\dot{u}_{n,1}^j & \Delta\dot{u}_{t,1}^j & \Delta\dot{u}_{n,2}^j & \Delta\dot{u}_{n,2}^j\end{bmatrix}^T\\&=\sum_{i\in I_j}\operatorname{sgn}\left(\left(\mathbf{r}_{j,1}^i+\mathbf{r}_{j,2}^i\right)\mathbf{e}_n^j\right)\left[\left(\mathbf{A}_{j,u}^i\right)^T\mathbf{u}^i+\left(\mathbf{A}_{j,\varepsilon}^i\right)^T\boldsymbol{\varepsilon}^i\right]\end{aligned} \tag{5}$$

$$I_j=\left\{i\,|\,\text{block } i \text{ is associated with joint } j\right\}$$

Then, we subtract velocities at the corresponding vertices in blocks a and b. The joint discontinuous can be derived by projecting such subtraction onto the local frame of the joint. The matrix form of this relation is given in Eq. (5).

The components in matrices $\mathbf{A}_{j,u}^i$ and $\mathbf{A}_{j,\varepsilon}^i$ are given in, which completely depend on the geometry of the elements.

$$\mathbf{A}_{j,u}^{i}=\begin{bmatrix} e_{n,x}^{j} & e_{n,y}^{j} & -y_1^i e_{n,x}^{j}+x_1^i e_{n,y}^{j} \\ e_{t,x}^{j} & e_{t,y}^{j} & -y_1^i e_{t,x}^{j}+x_1^i e_{t,y}^{j} \\ e_{n,x}^{j} & e_{n,y}^{j} & -y_2^i e_{n,x}^{j}+x_2^i e_{n,y}^{j} \\ e_{t,x}^{j} & e_{t,y}^{j} & -y_2^i e_{t,x}^{j}+x_2^i e_{t,y}^{j} \end{bmatrix}^T \quad \mathbf{A}_{j,\varepsilon}^{i}=\begin{bmatrix} x_1^i e_{n,x}^{j} & y_1^i e_{n,y}^{j} & y_1^i e_{n,x}^{j}+x_1^i e_{n,y}^{j} \\ x_1^i e_{t,x}^{j} & y_1^i e_{t,y}^{j} & y_1^i e_{t,x}^{j}+x_1^i e_{t,y}^{j} \\ x_2^i e_{n,x}^{j} & y_2^i e_{n,y}^{j} & y_2^i e_{n,x}^{j}+x_2^i e_{n,y}^{j} \\ x_2^i e_{t,x}^{j} & y_2^i e_{t,y}^{j} & y_2^i e_{t,x}^{j}+x_2^i e_{t,y}^{j} \end{bmatrix}^T \tag{6}$$

Assembling the geometric compatibility condition for all the joints, we can write the compatibility constraint in a global matrix form (Eq. (7)). Compared with the one for rigid elements [10], a term $\mathbf{A}_{\varepsilon}^{T}\boldsymbol{\varepsilon}$ is added to the compatibility condition, considering the deformability of the elements.

$$\mathbf{A}_{u}^{T}\mathbf{u}+\mathbf{A}_{\varepsilon}^{T}\boldsymbol{\varepsilon}=\mathbf{q} \tag{7}$$

Regarding the interfacial behavior, Mohr-Coulomb friction model is employed here (Eq. (8)) and the flow rule for the interfacial discontinuous velocities is associated with it. Thus, these velocities be represented through the involvement of plasticity multipliers (Eq. (9)).

$$\begin{aligned} & F\left(\overline{n},\overline{s}\right)=\overline{n}\sin\varphi+\left|\overline{s}\right|\cos\varphi-\frac{1}{2}c_0 A\cos\varphi\le 0 \\ \Leftrightarrow\ & F_k\left(\overline{n},\overline{s}\right)=\overline{n}\sin\varphi-(-1)^k\overline{s}\cos\varphi-\frac{1}{2}c_0 A\cos\varphi\le 0,\ k=1,2 \end{aligned} \tag{8}$$

$$\left.\begin{aligned} \Delta\dot{u}_{n,m} &= p_m\frac{\partial F}{\partial\overline{n}}=\sum_{k=1}^{2}p_m^k\frac{\partial F_k}{\partial\overline{n}}=p_m^{s+}\sin\varphi+p_m^{s-}\sin\varphi \\ \Delta\dot{u}_{t,m} &= p_m\frac{\partial F}{\partial\overline{s}}=\sum_{m=1}^{2}p_m^k\frac{\partial F_k}{\partial\overline{s}}=p_m^{s+}\cos\varphi-p_m^{s-}\cos\varphi \end{aligned}\right\},\ \left(m=1,2\right) \tag{9}$$

$$\Leftrightarrow\ \mathbf{N}^T\mathbf{p}=\mathbf{q},\ \ \mathbf{p}\ge 0$$

$$F\left(\sigma_x,\sigma_y,\tau_{xy}\right)=\sqrt{\left(\sigma_x-\sigma_y\right)^2+\left(2\tau_{xy}\right)^2}+\left(\sigma_x+\sigma_y\right)\sin\theta-2c_1\cos\theta\le 0 \tag{10}$$

$$F_k\left(\sigma_x,\sigma_y,\tau_{xy}\right)=A_k\sigma_x+B_k\sigma_y+2C_k\tau_{xy}-2c_1\cos\theta\le 0 \tag{11}$$

A flow rule associated with Mohr-Coulomb criterion for the continuum is also applied here to constrain the element strain rate [11]. Standard Mohr-Coulomb criterion (see Eq. (10)) is nonlinear and the corresponding flow rule cannot be written as a linear constraint. Thus, we follow the solution proposed in [12], linearizing this yield surface into *p* planes. The equation of the *k*th plane is given in Eq. (11), where coefficients A_k, B_k, and C_k are given in Eq. (12).

$$\begin{cases} A_k = \cos a_k + \sin\theta \\ B_k = \cos a_k - \sin\theta \ , \ a_k = 2\pi k/p \, , \ k = 1,2,\ldots,p \\ C_k = \sin a_k \end{cases} \tag{12}$$

According to the associativity, the plastic strain rate for each element is linked with k non-negative plastic multipliers (left side of Eq. (13)) and we can also write the equivalent matrix form collecting the variable for all the elements (right side of Eq. (13)).

$$\left.\begin{aligned} \dot{\varepsilon}_x &= \dot{\lambda}\frac{\partial F}{\partial \sigma_x} = \sum_{k=1}^{p}\dot{\lambda}_k\frac{\partial F_k}{\partial \sigma_x} = \sum_{k=1}^{p}\dot{\lambda}_k A_k \\ \dot{\varepsilon}_y &= \dot{\lambda}\frac{\partial F}{\partial \sigma_y} = \sum_{k=1}^{p}\dot{\lambda}_k\frac{\partial F_k}{\partial \sigma_y} = \sum_{k=1}^{p}\dot{\lambda}_k B_k \\ \dot{\varepsilon}_{xy} &= \frac{1}{2}\dot{\lambda}\frac{\partial F}{\partial \tau_{xy}} = \frac{1}{2}\sum_{k=1}^{p}\dot{\lambda}_k\frac{\partial F_k}{\partial \tau_{xy}} = \sum_{k=1}^{p}\dot{\lambda}_k C_k \end{aligned}\right\} \Leftrightarrow \mathbf{M}^T\dot{\boldsymbol{\lambda}} = \boldsymbol{\varepsilon},\ \dot{\boldsymbol{\lambda}} \geq 0 \tag{13}$$

The plastic dissipation at the interfaces $\dot{W}^c_{D,j}$ (for joint j) and elements $\dot{W}^e_{D,i}$ (for element i) can both be calculated from the inner product of the cohesion vector and plastic multiplier vector (Eq. (14)). Summing these over all the interfaces or elements, the global dissipation power at the interfaces and elements can be represented.

$$\begin{aligned} \dot{W}^c_{D,j} &= \Delta\dot{u}^j_{n,1} + \Delta\dot{u}^j_{n,2}\overline{n}^j_2 + \Delta\dot{u}^j_{t,1}\overline{s}^j_1 + \Delta\dot{u}^j_{t,2}\overline{s}^j_2 \\ &= p^{s+}_1\left(\overline{n}^j_1\sin\varphi + \overline{s}^j_1\cos\varphi\right) + p^{s-}_1\left(\overline{n}^j_1\sin\varphi - \overline{s}^j_1\cos\varphi\right) \\ &\quad + p^{s+}_2\left(\overline{n}^j_2\sin\varphi + \overline{s}^j_2\cos\varphi\right) + p^{s-}_2\left(\overline{n}^j_2\sin\varphi - \overline{s}^j_2\cos\varphi\right) \\ &= \frac{1}{2}c_{0,j}A_j\cos\varphi_j\left(p^{s+}_1 + p^{s-}_1 + p^{s+}_2 + p^{s-}_2\right) = \mathbf{c}^T_{0,i}\mathbf{p}_i \\ \dot{W}^e_{D,i} &= \int_V\left(\sigma_x\dot{\varepsilon}_x + \sigma_y\dot{\varepsilon}_y + 2\tau_{xy}\dot{\varepsilon}_{xy}\right)dV \\ &= \sum_{k=1}^{p}\int_V\left(\dot{\lambda}_k A_k\sigma_x + \dot{\lambda}_k B_k\sigma_y + 2\dot{\lambda}_k C_k\tau_{xy}\right)dV \\ &= 2c_{1,i}\cos\theta_i V_i\sum_{k=1}^{p}\dot{\lambda}_k = \mathbf{c}^T_{1,i}\dot{\boldsymbol{\lambda}}_i \end{aligned} \tag{14}$$

Taking into account the dissipation power in the objective function, we can establish an optimization formula Eq. (15) based on the UB theory. The terms in red are all related to the consideration of the deformability of the elements.

$$\begin{aligned} \text{minimize} \quad & -\mathbf{f}_D^T\mathbf{u} + \mathbf{c}_0^T\mathbf{p} + \mathbf{c}_1^T\dot{\boldsymbol{\lambda}} \\ \text{subject to} \quad & \mathbf{f}_L^T\mathbf{u} = 1 \\ & \mathbf{A}_u^T\mathbf{u} + \mathbf{A}_\varepsilon^T\boldsymbol{\varepsilon} = \mathbf{q} \\ & \mathbf{N}^T\mathbf{p} = \mathbf{q}, \mathbf{p} \geq 0 \\ & \mathbf{M}^T\dot{\boldsymbol{\lambda}} = \boldsymbol{\varepsilon}, \dot{\boldsymbol{\lambda}} \geq 0 \end{aligned} \tag{15}$$

3 Results: strip footing problem

As a verification of the proposed theory, we perform the collapse analysis of the plane strain strip footing. This benchmark is a classical problem in geomechanics and the analytical solution is available. In the work of Sloan and Kleeman [12], they predicted the collapse load of this problem through the limit analysis with a triangular discretization for the soil, and the result is consistent with the analytical solution. In this section, the collapse of the strip footing with the structured triangular discretization, which agrees with the one employed in the literature [12], is first presented as a benchmark. Then, we proceed to investigate the performance of the polygon mesh in analyzing this problem.

3.1 Benchmark: structured triangular mesh

We select the case of weightless cohesive-frictional soil, with surface pressure. To verify the proposed approach, the geometry, mesh, load, and boundary conditions are kept in line with the ones in Sloan and Kleeman (see [12]). The depth of the soil is 1000 mm. Triangular mesh with different refinements is first considered (**Fig. 2**). We also compare the result of different precision of linearization for the Mohr-Coulomb yield surface (p = 6, 12 and 24).

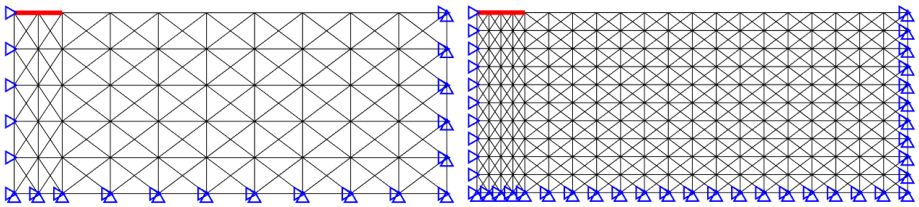

(a) coarse mesh (b) fine mesh

Fig. 2. Strip footing problem (refer to [12]), load and boundary conditions, triangular mesh.

Comparing the results of p = 6, 12 and 24 in **Fig. 3** and **Fig. 4**, we can find that increasing the number of planes will give rise to a better prediction. After employing more linearizing planes, the separation velocity among the element is reduced and the cracks spread in the continuum in a more uniform manner. The deformability of the element rises, with an exhibition of smoother distribution of the strain rate. The pre-

dicted collapse load is also more conservative. Such improvement in the prediction should be attributed to the fact that the Mohr-Coulomb surface is more precisely represented when linearizing planes increases.

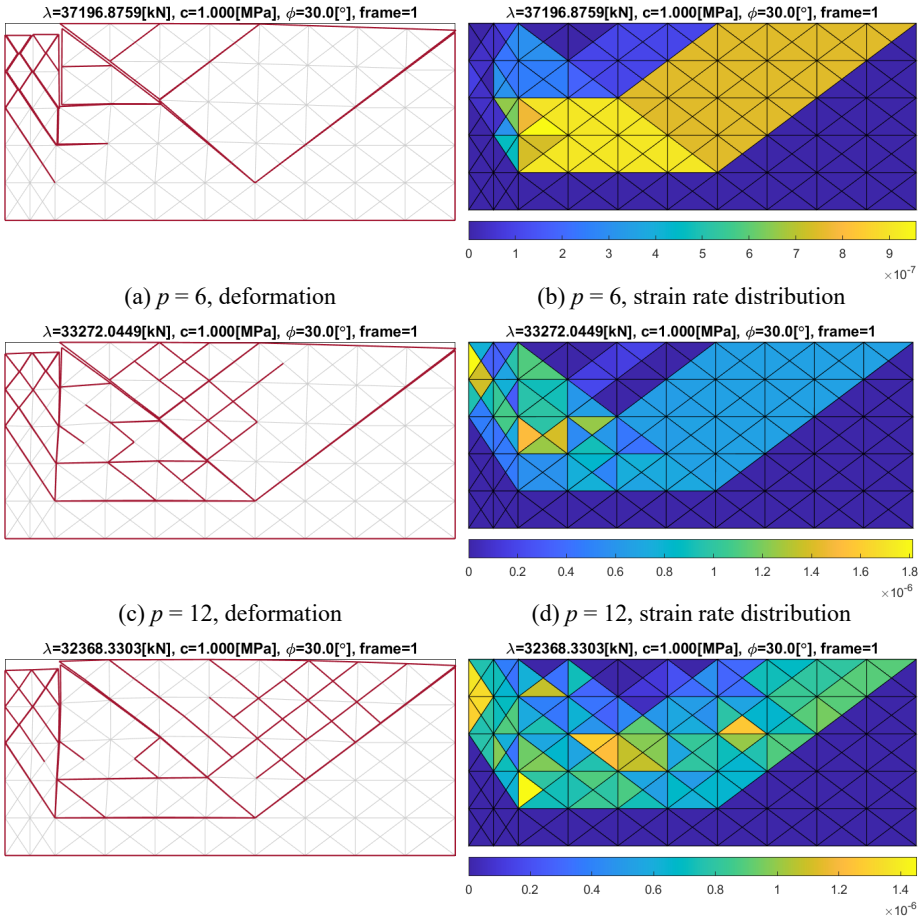

(a) $p = 6$, deformation (b) $p = 6$, strain rate distribution

(c) $p = 12$, deformation (d) $p = 12$, strain rate distribution

(e) $p = 24$, deformation (f) $p = 24$, strain rate distribution

Fig. 3. Collapse of the strip footing problem, triangular element, coarse mesh.

The collapse load will also decrease if the mesh is refined (compare **Fig. 3** and **Fig. 4**). Thanks to the employment of smaller elements, more detailed crack propagation in the continuum is produced. The representation of strain rate distribution is also improved because we only assume a constant strain rate field in each element. A refined mesh can accurately catch the change in the strain rate in the soil. Note that in this case, refining the linearization of the yield surface brings about a better improvement in the results rather than refining the mesh. Regarding the collapse load, reducing the element size will cut down only 0.6% of the prediction while the load presents a 14.7% drop when increasing the number of linearizing planes.

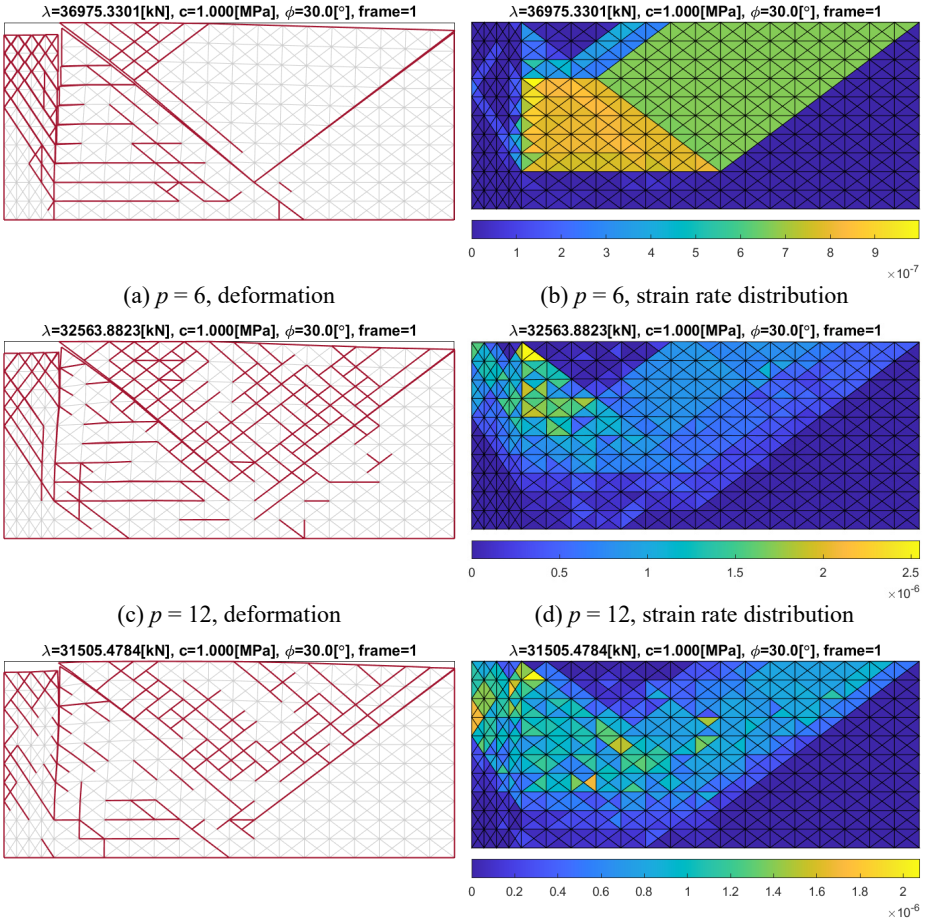

(a) $p = 6$, deformation (b) $p = 6$, strain rate distribution

(c) $p = 12$, deformation (d) $p = 12$, strain rate distribution

(e) $p = 24$, deformation (f) $p = 24$, strain rate distribution

Fig. 4. Collapse of the strip footing problem, triangular element, fine mesh.

According to the geomechanics, the Prandtl collapse pressure for a surface footing on a weightless cohesive-frictional soil is given in Eq. (16), where c and φ are, respectively, the effective cohesion and friction angle. In this analysis, we keep the $\varphi = 30°$ and $c = 1$ MPa, which is the same as the parameter set in [12]. The exact solution for q_f is 30.14 MPa.

$$q_f = N_c c = \cot\varphi\left(e^{\pi\tan\varphi}\tan^2\left(\pi/4+\varphi/2\right)-1\right)c \tag{16}$$

The collapse load predicted by triangular mesh and polygon mesh presented above is summarized in **Table 1**. Here, $q_{f,\mathrm{tri}}$ is the collapse load predicted by the structured triangular mesh; $q_{f,s}$ is the result reported in [12]; q_f is the accurate value calculated by

the analytical solution. In the triangular case, the results produced by the proposed approach are basically consistent with the prediction in [12], verifying that the presented theory can give a correct solution to the strip footing problem.

Table 1. Results for strip footing on cohesive-frictional, structured triangular mesh.

Mesh size	p	$q_{f,\mathrm{tri}}$ (MPa)	$q_{f,\mathrm{tri}}$ error (%)	$q_{f,s}$ (MPa)	$q_{f,s}$ error (%)	q_f (MPa)
Coarse mesh	6	37.20	23.4	37.26	23.6	30.14
Fine mesh	6	36.98	22.7	37.04	22.9	
Coarse mesh	12	33.27	10.4	33.36	10.7	
Fine mesh	12	32.56	8.0	32.67	8.4	
Coarse mesh	24	32.37	7.4	32.70	8.5	
Fine mesh	24	31.51	4.5	31.75	5.4	

3.2 Polygon mesh case

Then, the collapse of this problem where the soil is discretized by the polygon elements is analyzed to understand the performance of the proposed elements. Polygon mesh is produced based on Voronoi tessellation. Two types of Voronoi mesh are considered: a) random Voronoi mesh, where the shape of the polygon is more random (**Fig. 5**a); b) centroid Voronoi mesh, where the shape of the polygon is more regular (**Fig. 5**b). Both these two meshes are generated through an open-source code "lloydsAlgorithm" [13]. Here we do not consider the different element sizes. The numbers of the element for Random Voronoi and Centroid Voronoi mesh are both 1125. The characteristic size of the elements is about 210 mm.

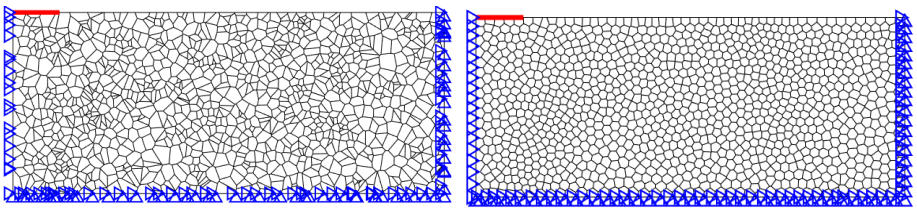

(a) Random Voronoi mesh (b) Centroid Voronoi mesh

Fig. 5. Strip footing problem with polygon mesh, load and boundary conditions.

In the polygon mesh case, we also find that a better prediction will be obtained if the number of linearizing planes increases. Not only is the distribution of the strain rate more smooth, but the predicted collapse load also becomes safer. This regulation agrees with the observation in the triangular case. Increasing from 6 to 24, the load drops about 26.5 – 31.8 %.

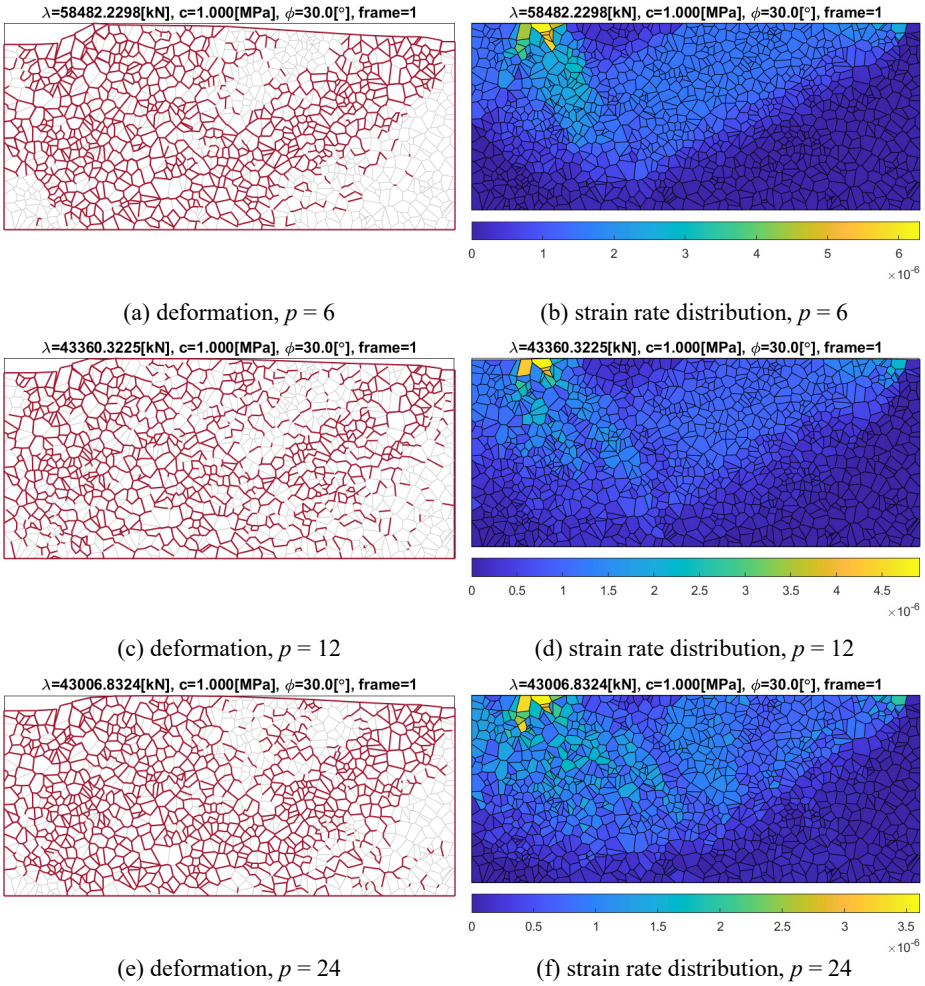

(a) deformation, $p = 6$ (b) strain rate distribution, $p = 6$

(c) deformation, $p = 12$ (d) strain rate distribution, $p = 12$

(e) deformation, $p = 24$ (f) strain rate distribution, $p = 24$

Fig. 6. Collapse of the strip footing problem, polygon element, random Voronoi mesh.

Comparatively, the centroid Voronoi mesh predicts a more uniform distribution of the strain rate than the random Voronoi mesh (compare **Fig. 6** and **Fig. 7**). While the collapse load predicted by centroid Voronoi mesh is slightly higher (about 7 – 14 %). The deformation and the spreading of the cracks predicted by these two polygon meshes are basically in line with each other.

Collapse loads predicted by polygon mesh are all higher than the one in the triangular case (see **Fig. 3** and **Fig. 4**), indicating that a locking phenomenon may take place in the element or at the interfaces. The locking at the interfaces should be caused by the shape of the element. No possible straight cracking can happen among polygon elements. As a result, the interaction between the elements tends to be extrusion instead of frictional sliding. Thus, we can observe a large number of cracks spreading within the whole continuum body. Oppositely, the separation between the

elements is not very obvious. Another part of the locking happens within the element, which should result from the assumption of constant strain distribution. For the triangular element, the number of nodal degrees (3 nodes and two velocities for each) is equal to the number of centroid variables (6, see Eq. (4)). While in the polygon case, nodal freedom increases but the number of centroid variables remains at 6. This means that in the polygon element, the velocity at each node is not independent. In other words, they are locked with each other to some extent, which makes the proposed polygon element behave physically stiffer than the triangular element. This also explains why polygon mesh predicts a larger collapse load.

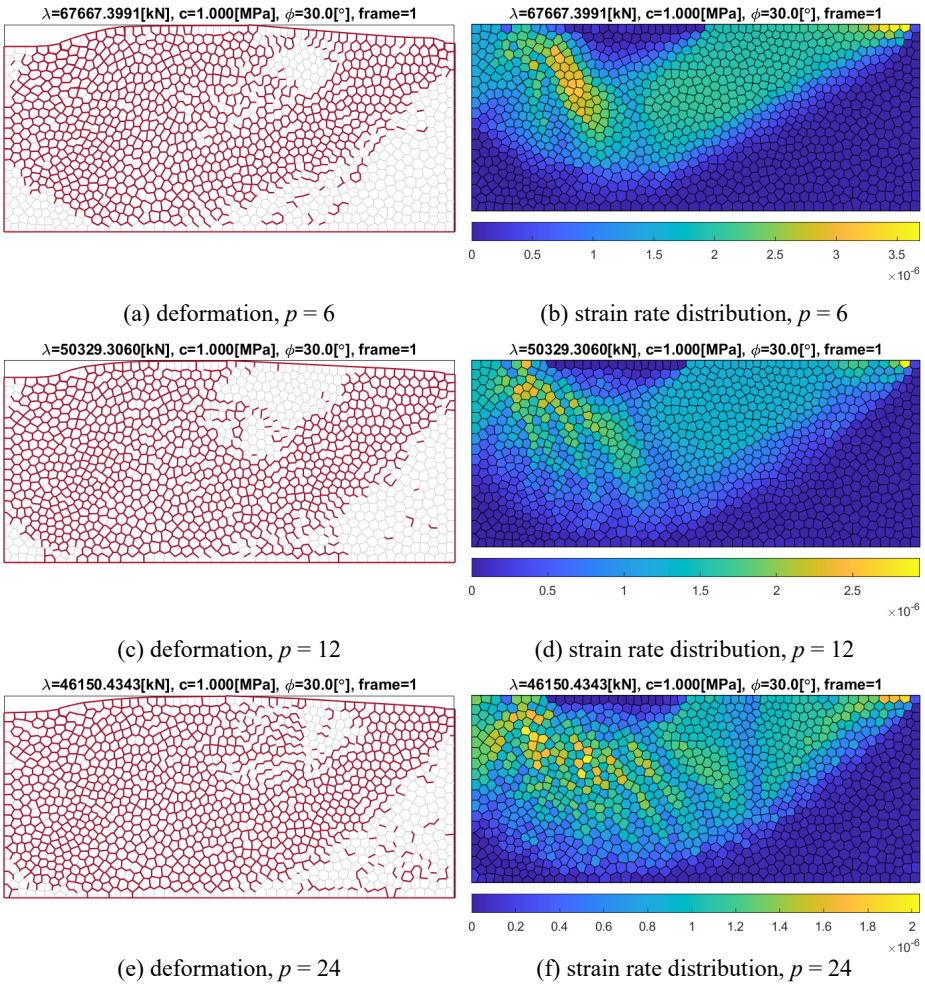

(a) deformation, $p = 6$ (b) strain rate distribution, $p = 6$

(c) deformation, $p = 12$ (d) strain rate distribution, $p = 12$

(e) deformation, $p = 24$ (f) strain rate distribution, $p = 24$

Fig. 7. Collapse of the strip footing problem, polygon element, centroid Voronoi mesh.

The collapse load predicted by two types of polygon mesh is collected in **Table 2**. $q_{f,\text{poly}}$ represents the collapse load predicted by the polygon mesh. The load predicted

by polygon mesh is about 36 – 83% greater than the accurate solution, which again indicates the locking phenomenon may occur. In addition, note that if the precision of the linearization for the yield surface is improved, the locking in the elements will be reduced to some extent.

Table 2. Results for strip footing on cohesive-frictional, polygon mesh.

Mesh type	p	$q_{f,\mathrm{poly}}$ (MPa)	$q_{f,\mathrm{poly}}$ error (%)	$q_{f,\mathrm{tri}}$ (MPa)	$q_{f,\mathrm{tri}}$ error (%)	q_f (MPa)
Random Voronoi	6	58.48	94.0	36.98	22.7	30.14
Centroid Voronoi	6	67.67	124.5			
Random Voronoi	12	43.36	43.9	32.56	8.0	
Centroid Voronoi	12	50.33	67.0			
Random Voronoi	24	43.01	42.7	31.51	4.5	
Centroid Voronoi	24	46.15	53.1			

4 Conclusions

In this paper, we have proposed a deformable polygon element with constant-strain distribution for the discretization of soil when using the limit analysis. The formulation is established based on the Upper Bound theory. We have first updated the geometric compatibility condition to consider the deformability of the element, and the associated Mohr-Coulomb flow rule is then employed for modeling the plastic deformation in these elements. Implementing the proposed theory, the collapse analysis of the classical strip footing problem has been presented as a benchmark. We have repeated the structured triangular case that has been analyzed by previous researchers to verify the accuracy of the proposed theory. After that, the performance of different polygon discretization has been compared.

The results of the triangular-mesh case show that, when analyzing the strip footing, the presented theory can give consistent predictions to the simulation in the previous contribution, verifying the accuracy of the approach. The load predicted by polygon mesh presents an overestimation of about 36 – 83%, which indicates that, in this problem, the proposed elements may suffer from interior locking. In other words, the deformable polygon element is stiffer than the triangular one under the same condition of the mesh size. However, the distribution of the strain rate predicted by the polygon mesh is more uniform. According to our study, employing the polygon with a more regular shape will give rise to a better prediction of strain rate distribution, while the predicted load may be slightly higher (see the case of Centroid Voronoi mesh). Refining the linearization of the yield surface in both triangular and polygon cases will bring about a more conservative prediction of the ultimate load.

Future work will concern how to reduce the locking of the polygon element for better performance. We will also apply the proposed theory to different types of problems, investigating such locking phenomena under different boundary conditions. The applicability of the proposed element may then be concluded.

References

1. Milani G., Lourenço P.B. A discontinuous quasi-upper bound limit analysis approach with sequential linear programming mesh adaptation. Int J Mech Sci 51, 89–104 (2009). https://doi.org/10.1016/j.ijmecsci.2008.10.010
2. Lyamin A. V., Sloan S.W. Upper bound limit analysis using linear finite elements and non-linear programming. Int J Numer Anal Methods Geomech 26, 181–216 (2002). https://doi.org/10.1002/nag.198.
3. Tschuchnigg F., Schweiger H.F., Sloan S.W. Slope stability analysis by means of finite element limit analysis and finite element strength reduction techniques. Part II: Back analyses of a case history. Comput Geotech 70, 178–189 (2015). https://doi.org/10.1016/j.compgeo.2015.07.019.
4. Tin-Loi F., Ngo N.S. Performance of the p-version finite element method for limit analysis. Int J Mech Sci 45, 1149–1166 (2003). https://doi.org/10.1016/j.ijmecsci.2003.08.004.
5. Gilbert M., Nguyen D., Smith C. Computational limit analysis of soil-arch interaction in masonry arch bridges. In: Proc 5th Int Conf arch Bridg ARCH, pp. 633–640 (2007).
6. Cavicchi A., Gambarotta L. Two-dimensional finite element upper bound limit analysis of masonry bridges. Comput Struct 84 ,2316–2328 (2006). https://doi.org/10.1016/j.compstruc.2006.08.048
7. Cavicchi A., Gambarotta L. Collapse analysis of masonry bridges taking into account arch-fill interaction. Eng Struct 27, 605–615 (2005). https://doi.org/10.1016/j.engstruct.2004.12.002
8. Milani G., Lourenço P.B. 3D non-linear behavior of masonry arch bridges. Comput Struct 110–111, 133–150 (2012). https://doi.org/10.1016/j.compstruc.2012.07.008
9. Papa T., Grillanda N., Milani G. Three-dimensional adaptive limit analysis of masonry arch bridges interacting with the backfill. Eng Struct 248, 113189 (2021). https://doi.org/10.1016/j.engstruct.2021.113189
10. Ferris M.C., Tin-Loi F. Limit analysis of frictional block assemblies as a mathematical program with complementarity constraints. Int J Mech Sci 43, 209–224 (2001). https://doi.org/10.1016/S0020-7403(99)00111-3
11. Sloan S.W., Kleeman P.W. Upper bound limit analysis using discontinuous velocity fields. Comput Methods Appl Mech Eng 127, 293–314 (1995). https://doi.org/10.1016/0045-7825(95)00868-1
12. Bottero A, Negre R, Pastor J, Turgeman S. Finite element method and limit analysis theory for soil mechanics problems. Comput Methods Appl Mech Eng 22, 131–149 (1980). https://doi.org/10.1016/0045-7825(80)90055-9
13. Aaron T. Becker's Robot Swarm Lab. lloydsAlgorithm(Px,Py, crs, numIterations, showPlot), MATLAB Central File Exchange. Retrieved April 5, (2023). https://www.mathworks.com/matlabcentral/fileexchange/41507-lloydsalgorithm-px-py-crs-numiterations-showplot